Biomedicine & Pharmacotherapy 189 (2025) 118287

Contents lists available at ScienceDirect

Biomedicine & Pharmacotherapy

journal homepage: www.elsevier.com/locate/biopha

Bone marrow tumor microenvironment profiling predicts distinct immunosuppressive phenotypes and immunotherapy potential in AML patients

Leslie Correia da Cruz [a,1], Yejin Lee [b], Ji Yeon Paik [b], Jeonghye Park [b], Marc Diederich [b,*,2,3], Claudia Cerella [a,*,2,4,5]

[a] Laboratoire de Biologie Moléculaire du Cancer, BAM3 Pavillon 2, 6A rue Nicolas-Ernest Barblé, Luxembourg L-1210, Luxembourg
[b] Research Institute of Pharmaceutical Sciences & Natural Products Research Institute, College of Pharmacy, Seoul National University, Seoul 08826, Republic of Korea

ARTICLE INFO

Keywords:
TME archetypes
AML immunoprofiling
Differentiation biomarkers

ABSTRACT

The immune landscape of acute myeloid leukemia (AML) is poorly understood, and its myeloid origins complicate the distinction between pathological and immunoregulatory components. We refined the AML microenvironment (AME) classification, demonstrating distinct immunophenotypes from AML lineages and maturation stages. We developed distinct 13-gene megakaryocytic/erythroid (MK/Ery) and 16-gene myelomonocytic/monocytic (ML/Mo) polygenic markers and validated them in adult and pediatric AML patient cohorts, including single-cell RNA-sequencing data. To identify immunoregulatory factors, the AME composition was predicted by the xCell algorithm, immune dysfunction was computed by TIDE, and differential gene expression analyses identified candidate genes. To validate our findings, we studied the effects of MK/Ery-like and ML/Mo-like AML cell lines on $CD8^+$ T-cells/AML cells in co-culture assays, using models identified by Celligner matching AML patient blasts. Patients with high MK/Ery expression (MK/Ery^{High}) exhibited a dysfunctional microenvironment with increased pro-inflammatory cytokines, increased T-cell infiltration, and upregulated immune checkpoints, particularly CD274 (PD-L1). Single-cell RNA-seq confirmed that CD274 overexpression originated from malignant subclones with MK/Ery-like phenotypes. Conversely, AML with high ML/Mo expression (ML/Mo^{High}) displayed a T-cell-depleted niche enriched in myeloid-derived suppressive elements, including M2 macrophages, VISTA, and galectins. MK/Ery-like (e.g., OCI-M1, HEL) and ML/Mo-like (e.g., MUTZ3, MONO-MAC-1) cells suppressed T-cell proliferation in co-culture. Pharmacological PD-1/PD-L1 blockade with the small-molecule inhibitors BMS-1166 and BMS-1001 abrogated HEL-mediated T-cell proliferation inhibition. Transcriptomic data, single-cell analyses, and functional co-culture experiments reveal two AMEs: T–cell–rich yet dysfunctional vs. myeloid-driven and immunosuppressive. This refined categorization overcomes the traditional hot–cold classification to tailor future AML immunotherapies.

1. Introduction

Acute myeloid leukemia (AML) is a hematologic malignancy characterized by high therapy resistance and recurrence rates, leading to poor prognosis. Compelling evidence indicates that AML blasts can actively suppress the immune system. Various factors, including blast maturation stage [1], inflammatory signaling [2], and metabolic rewiring [2], suppress T-cell immunity [3].

While immunotherapy has significantly improved outcomes in solid tumors, progress in AML has been limited. Clinical trials assessing

* Corresponding authors.
E-mail addresses: marcdiederich@snu.ac.kr (M. Diederich), claudia.cerella@lbmcc.lu, claudia.cerella@lih.lu (C. Cerella).
[1] Present address: Hematology Laboratory, GIGA, University of Liège, Avenue de l'Hôpital, 1, 4000 Liège, Belgium.
[2] Equal contribution.
[3] 0000-0003-0115-4725
[4] Present address: Department of Cancer Research, Luxembourg Institute of Health (LIH), BAM Pavillon 2, 6A rue Nicolas-Ernest Barblé, L-1210 Luxembourg, Luxembourg.
[5] 0000-0001-9308-8176

https://doi.org/10.1016/j.biopha.2025.118287
Received 12 February 2025; Received in revised form 14 June 2025; Accepted 20 June 2025
Available online 23 June 2025

immune checkpoint inhibitors (ICIs) in AML and myelodysplastic syndrome (MDS) have produced inconsistent results. Furthermore, efforts to develop T-cell adaptive therapies for AML have not been sufficient. The response to ICIs has traditionally been linked to a high tumor mutational burden (TMB), which expands the neoantigen repertoire and increases T-cell infiltration into the tumor microenvironment (TME), creating a so-called "hot" tumor.

Because AML blasts exhibit a low TMB and bone marrow (BM) biopsies from AML patients show lower T-cell abundance compared to age-matched healthy donors, AML has generally been considered to have a T–cell-depleted ("cold") TME, making it intrinsically refractory to ICIs and T–cell–targeting therapies. Enhancing the immunogenicity of AML blasts through immunogenic cell death-based vaccination has been suggested as one strategy to address these limitations.

Notably, subsets of adult and pediatric AML patients exhibit BM T-cell levels comparable to non-leukemic controls, and other studies have identified lymphoid aggregates within the BM [4]. These findings suggest that profiling the complexity of the AML TME could improve prognostic stratification and help identify patients who may benefit from immunomodulatory therapies.

Considering that the classical "hot versus cold" framework oversimplifies the dynamic and heterogeneous immune environment found in AML and the important association emerging from recent studies between AML blast maturation and altered immune-related pathways, we hypothesize that AML subtypes with distinct differentiation states [1], particularly those exhibiting megakaryocytic/erythroid (MK/Ery) or myelomonocytic/monocytic (ML/Mo) features, give rise to unique immunosuppressive niches. Instead of adhering to a binary hot-cold classification, these niches extend our knowledge by combining information on T-cell infiltration, T-cell exhaustion, myeloid-driven immunosuppression, and variable antigen presentation.

This study systematically examines transcriptomic, mutational, and TME data across AML cohorts and cell lines to redefine TME cellular and functional complexity built on differentiation-based subgroups. AML patients with an MK/Ery signature exhibit stem-like traits, myelodysplastic-related changes (MRC-AML), TP53 mutations, and a T-cell–infiltrated yet dysfunctional TME with high PD-L1 expression. In contrast, ML/Mo AML features a T-cell–depleted TME, enriched M2 macrophages, high MHC subunit expression, and immunosuppressive factors such as V-domain Ig suppressor of T-cell activation (VISTA), galectins, and T-cell immunoglobulin and mucin domain-containing protein 3 (TIM-3).

Bristol-Myers Squibb's small-molecule ICIs BMS-1001 and BMS-1166 were developed as chemical probes of the PD-1/PD-L1 axis. These compounds are low-nanomolar binders that efficiently release T-cell receptor signalling in vitro without intrinsic cytotoxicity [5]. Although antibody-based PD-1/PD-L1 blockade has achieved limited responses in AML, small-molecule ICIs provide an interesting tool to dissect checkpoint-mediated immunosuppression in co-culture systems. We used BMS-1001 and BMS-1166 to determine whether pharmacologic PD-L1 blockade can restore primary T-cell proliferation suppressed by co-culture with the MK/Ery-type AML cell line HEL.

Our results reveal contrasting T-cell–rich yet dysfunctional milieus in MK/Ery^{high} AML versus T-cell–depleted but highly myeloid-infiltrated environments in ML/Mo^{high} AML. Since immunotherapeutic intervention with small-molecule PD-L1 inhibitors BMS-1166 and BMS-1001 eliminated the inhibition of T-cell proliferation mediated by HEL, our results are paving the way for a more refined classification of AML immune phenotypes, with direct implications for therapeutic targeting.

2. Materials and methods

2.1. Publicly available datasets and bioinformatics web tools

Data from various publicly available adult and pediatric AML patient cohorts and the Cancer Cell Line Encyclopedia (CCLE) AML cell line dataset [6] were used in this study (Table S16). Only non-redundant AML patient samples at diagnosis were selected for analysis, as previously indicated [7]. Data processing and analysis employed various methods, including the DESeq2 R package for RNA-Seq count matrix analysis, robust multichip average (RMA) normalization for microarray data, Seurat package for single-cell RNA-Seq data, and Bioconductor R software for differential gene expression analysis and data visualization (R Studio Version 4.3.3, 2023.12.1 +402). Further details on these methods and additional bioinformatics tools used in this study are provided in the following sections. Clinical patient data and processed expression data were retrieved from cBioPortal [8] (https://www.cbioportal.org) and XenaBrowser [9] (https://xenabrowser.net).

The results of The Cancer Genome Atlas (TCGA) AML cohorts are based in whole or in part on data generated by the TCGA Research Network (https://www.cancer.gov/tcga) and by the Therapeutically Applicable Research to Generate Effective Treatments (TARGET) initiative (https://www.cancer.gov/ccg/research/genome-sequencing/target), phs000218 [10]. Data used in this analysis were accessed through the Genomic Data Commons (https://portal.gdc.cancer.gov). XenaBrowser (https://xenabrowser.net) was used to retrieve processed RNA-Seq gene expression data (log2(FPKM-uq+1)) and clinical information. The analysis included 145 non-redundant patient specimens collected at diagnosis [7].

Pediatric cancer data were retrieved from the open-access St. Jude Cloud (PeCan initiative, https://pecan.stjude.cloud) [11]. Processed expression values (FPKM) for the genes of interest and disclosed clinical information were downloaded from the PeCan platform. Only specimens collected at diagnosis were included, while those with redundant ID codes were excluded to avoid sample duplication. The final dataset comprised N = 305 pediatric AML samples.

Beat AML2 cohort data [12] were retrieved from the Vizome database (http://www.vizome.org/aml2/). Additionally, cBioPortal was used to access processed RNA-Seq gene expression data (log2RPKM) and clinical information from the dataset OHSU, Cancer Cell 2022 [12]. The analysis included 596 non-redundant patient specimens collected at diagnosis or the earliest follow-up, as previously specified [7].

Some results presented in this publication are based on data from the Leucegene group, primarily located at the Institute for Research in Immunology and Cancer (IRIC) in Montreal, Canada, and supported by Genome Canada and Genome Québec. These data were obtained from human AML specimens provided by the Banque de cellules leucémiques du Québec (BCLQ) in Montreal, Canada. RPKM data for the Leucegene cohort were retrieved from the Gene Expression Omnibus (GEO) database (GSE49642, GSE52656, GSE62190, GSE66917, GSE67039). The GSM ID numbers were matched with respective patient IDs, and gene expression values were integrated with clinical features disclosed in publications by the Leucegene group [13–17]. As with other cohorts, only non-redundant AML samples collected at diagnosis were included (N = 387) [7].

Single-cell RNA-Seq datasets (matrix.mtx.gz, features.tsv.gz, barcodes.tsv.gz) from two AML patients analyzed in the Kuusanmäki et al. study [18] - namely AML-1 (peripheral blood, megakaryocytic differentiation) and AML-5 (bone marrow, erythroid differentiation) - were retrieved from the EMBL-EBI database (BioStudies/ArrayExpress; https://www.ebi.ac.uk/biostudies/arrayexpress/studies/E-MTAB-12607). Data were analyzed using Seurat (version 5.1.0) in R, and cells with > 10 % mitochondrial reads, fewer than 200 genes, or more than 2500 genes were excluded. Automated reference-based cell type annotation was applied using SingleR [19] (version 2.4.1; https://bioconductor.org/packages/devel/bioc/vignettes/SingleR/inst/doc/SingleR.html#References), and the FindMarkers function in Seurat.

Raw (.CEL) files and clinical data for 461 AML patients from the Verhaak et al. study (GSE6891) [20] were downloaded from GEO to process microarray datasets. Processed expression data from the CCLE AML cell line dataset [6] were retrieved from the DepMap Portal [21], with dataset versions and platforms specified in the following sections

(Table S16).

The percentage of T-cells out of 35 different cell types annotated from BM specimens of eight healthy donors was retrieved from the Human Cell Atlas Bone Marrow Single-Cell Interactive Web Portal [22].

ShinyGo (V.0.81) [23] was used to compute and visualize Hallmarks and KEGG gene ontology pathways for the selected cohorts. As input, genes with significant modulation (log2 fold change threshold: < -0.3 or > 0.3; p-adj value: < 0.05) were selected. Gene Set Enrichment Analysis (GSEA) was performed using GSEA 4.3.2 software (https://www.gsea-msigdb.org/gsea/index.jsp) with the following gene set databases: h.all.v2024.1Hs.symbols; Human_Ensembl_Gene_ID_MSigDB.v2024.1.Hs.chip; Human_Gene_Symbol_with_Remapping_MSigDB.v2024.1.Hs.chip.

Precomputed TME cell type enrichment analysis for TCGA LAML and TARGET AML cohorts was downloaded from xCell (https://comphealth.ucsf.edu/app/xcell) [24].

2.2. Polygenic Megakaryoblastic/Erythroid (MK/Ery) and Myelomonocytic/Monocytic (ML/Mo) markers

Representative genes for the MK/Ery and ML/Mo phenotypes were selected based on previous studies, including our own (Table S1) [7,18,25,26].

Expression values for these genes were extracted from publicly available AML patient datasets. The Z-score for each gene in each sample was calculated using the formula (gene X: log2 expression value for one sample - mean of log2 values of all samples) / standard deviation of log2 values of all samples). A Z-score polygenic mean was computed for both MK/Ery and ML/Mo differentiation signatures.

The MK/Ery signature was trained on the pediatric AML PeCan cohort (Hg38; FPKM values; non-redundant samples at diagnosis; N = 305; https://pecan.stjude.cloud) and the CCLE AML cell line dataset (N = 42, RPKM values; Table S2, https://depmap.org/portal/ccle/). The ML/Mo polygenic marker is based on genes validated in our previous study of myelomonocytic/monocytic AML phenotype characterization.

Two-sided Spearman's correlations were calculated between the MK/Ery Z-score polygenic mean and the Z-score for the genes of interest. Statistical analyses were performed using GraphPad Prism and the R "corrplot" package (https://github.com/taiyun/corrplot) for data visualization.

2.3. TME cell abundance prediction of cell line-proximal AML blasts

To identify AML patient samples from the TCGA LAML and TARGET AML cohorts that most closely resembled the OCI-M1, HEL, and MONO-MAC-1 cell lines, UMAP coordinates for both cell lines and AML specimens, computed using the Celligner algorithm (unsupervised alignment method) were retrieved from data 1 of the original publication [27] (https://depmap.org/portal/celligner/). The Euclidean distance (ED) between each cell line and each AML patient specimen in the TCGA LAML (N = 173) or TARGET AML (N = 145) cohorts was calculated. AML patient quartiles corresponding to the most proximal (low ED values) or distant (high ED values) samples to each cell line were selected for further analyses.

Alternatively, AML patients were categorized by MK/Ery or ML/Mo polygenic marker expression, and the top and bottom quartiles of expression were selected for comparative analysis of TME cell type abundance. Samples from BM sources were selected for these analyses.

Precomputed TME cell type enrichment analysis for the TCGA LAML and TARGET AML cohorts was downloaded from the xCell platform [24] (https://comphealth.ucsf.edu/app/xcell). Statistical evaluation of differential TME cell type abundance between cell line-proximal (proxy) and distant AML specimen groups was performed using the Mann-Whitney test (non-parametric, two-sided).

2.4. T-cell functional status prediction

The MK/Ery gene list was analyzed using the Tumor Immune Dysfunction and Exclusion (TIDE) algorithm [28] (http://tide.dfci.harvard.edu). This tool computed the T-cell immune dysfunction score for each MK/Ery gene listed in Table S1. The analysis included CD274 and BCL2L1 as controls, with CD274 linked to immunosuppression and BCL2L1 associated with erythroid/megakaryocytic differentiation [18].

2.5. Experimental cell models and culture conditions

2.5.1. Cell models

Established AML cell lines were obtained from the Deutsche Sammlung von Mikroorganismen und Zellkulturen (DSMZ, Braunschweig, Germany) (Table S17). All cell lines were purchased between late 2023 and early 2024, except for MUTZ-3 and 5637 (purchased in 2021) and F36P. Cell maintenance was performed every three to four days under conditions that allowed exponential growth, per the manufacturer's instructions. Monthly mycoplasma testing was conducted using the MycoAlert Assay Control Set and the Mycoplasma Detection Kit (Lonza, Basel, Switzerland).

Cell line authenticity and purity were regularly verified via DNA profiling using 17 highly polymorphic Short Tandem Repeat (STR) loci, alongside screening for mitochondrial DNA sequences of rodent species (mouse, rat, Chinese hamster, and Syrian hamster) (DSMZ, October 2020).

Peripheral blood mononuclear cells (PBMCs) were isolated from healthy adult donors through the Luxembourg Red Cross, with informed consent and ethical approval from the Red Cross Ethical Committee (Authorization Numbers: LBMCC-2019–0001; LBMCC-2019–0002).

2.5.2. T-cell isolation from healthy donor PBMCs

PBMCs were isolated from donated buffy coats via density gradient centrifugation using Ficoll-Paque (GE Healthcare Bio-Sciences, Uppsala, Sweden), as previously described [7,29,30]. PBMCs were seeded at 2×10^6 cells/ML in RPMI 1640 (Capricorn Scientific, Westburg B.V, Leusden, The Netherlands) medium supplemented with 10 % fetal bovine serum (FBS) and 1 % antibiotic/antimycotic (Capricorn Scientific, Westburg). After overnight incubation at 37°C and 5 % CO_2, T-cells were isolated using the Pan T-Cell Isolation Kit (Miltenyi Biotec, Bergisch Gladbach, Germany). T-cell purity (>90 %) was confirmed via flow cytometry (LSRFortessa™ X-20, BD Biosciences, Erembodegem, Belgium). See Table S18 for reagents and antibody details.

2.5.3. Co-culture assay

Cell proliferation was monitored over 72 h in activated T-cells. The cells were stained using the CellTrace™ Violet Cell Proliferation Kit (Thermo Fisher Scientific, Merelbeke, Belgium) following a modified protocol based on the manufacturer's instructions. Dynabeads™ Human T-Activator CD3/CD28 (Thermo Fisher Scientific), which mimics antigen-presenting T-cell receptor (TCR) stimulation, was used to activate T-cells. A total of 1×10^5 beads per assay were washed with 0.1 % bovine serum albumin (BSA, Sigma-Aldrich) and 2 mM ethylenediaminetetraacetic acid (EDTA, Sigma-Aldrich) in Dulbecco's Phosphate-Buffered Saline (PBS, BioWhittaker®, Verviers, Belgium). The beads were then mixed with 1×10^5 AML cells and 1×10^5 T-cells (maintaining a 1:1:1 ratio) in a total volume of 200 µl of the corresponding AML culture media (Table S1). Following gentle vortexing, each sample was aliquoted into four wells of a V-bottom 96-well plate (Greiner Labotechnik, Wemmel, Belgium) to prevent hypoxia and excessive cell clumping or overgrowth at the bottom of the wells. T-cells incubated only with beads served as positive controls for T-cell stimulation. Unstained and unstimulated T-cell samples (each containing 1×10^5 cells) were seeded into individual plate wells at a concentration of 1×10^5 cells per 200 µl for flow cytometry compensation settings. The plates were then incubated at 37°C, 5 % CO_2, and 95 % humidity for 72 h

before further assessments.

2.5.4. Co-culture with HEL cells and PD-L1 blockade

HEL cells were resuspended in complete RPMI 1640 medium supplemented with 10 % fetal bovine serum (FBS), 2 mM L-glutamine, 100 U/ML penicillin, and 100 μg ML streptomycin. Carboxyfluorescein succinimidyl ester (CFSE)-labeled T-cells (1×10^5 cells per sample) were co-seeded with HEL cells at a 1:1 ratio [31]. Each sample was aliquoted into four wells of a V-bottom-shaped 96-well plate (Greiner, GeneClone, Seoul, South Korea). Where indicated, cultures received either BMS-1166 (1.2 μM) or BMS-1001 (1.2 μM), dissolved in dimethyl sulfoxide (DMSO). Vehicle control wells contained 0.1 % (v/v) DMSO. Plates were incubated for 72 h at 37 °C, 5 % CO_2, and 95 % humidity. Cells were harvested, washed twice with PBS, and stained for 20 min in the dark at room temperature (RT) with anti-CD33 and anti-CD8 antibodies (see Table S18 for technical details). 0.5 μM SYTOX™ Deep Red Nucleic Acid Stain (Invitrogen™, Thermo Fisher Scientific, GeneClone, Seoul, South Korea) was added to each sample, followed by incubation for 15 min at RT in the dark in 200 μl RPMI 1640 medium without phenol red (Capricorn Scientific, Westburg). Single-stained T-cells and their respective isotype controls were prepared for each fluorophore (Table S18). Each sample underwent cytometry analysis with FACSLyric™ (BD Biosciences Korea, Seoul, South Korea). Data was acquired using BD FACSuite™ software (BD Biosciences) and subsequently analyzed with FlowJo v10 software. BMS-1166 and BMS-1001 were purchased from TargetMol (GeneClone, Seoul, South Korea), dissolved in DMSO to 1 mM stock solutions, and stored at −80 °C.

2.5.5. Flow cytometry analysis and gating strategy

After 72 h of stimulation, the samples were washed with PBS. The cell pellets were then incubated with a pre-prepared mixture of anti-CD33 and anti-CD8 antibodies (see Table S18 for technical details) for 20 min in the dark at room temperature (RT). At the end of the incubation, 0.5 μM SYTOX™ Deep Red Nucleic Acid Stain (Invitrogen™, Thermo Fisher Scientific) was added to each sample as a viability dye, followed by incubation for 15 min at RT in the dark in 200 μl RPMI 1640 medium without phenol red (Capricorn Scientific, Westburg). Single-stained T-cells and their respective isotype controls were prepared for each fluorophore (Table S18). Each sample underwent cytometry analysis until 10,000 events were recorded using an LSRFortessa™ X-20 (BD Biosciences). Data was acquired using BD FACSDiva™ software (BD Biosciences) and subsequently analyzed with FlowJo v10 software. A sequential gating strategy was applied to identify and monitor T-cell activation and proliferation, as depicted in Fig. 4**A**.

2.5.6. Dry and wet lab CD274 expression analysis

The CD274 mRNA gene expression data for 42 AML cell lines were downloaded from the DepMap Portal (Table S2; log2(TPM+1); version: 24Q4 Expression Public). These values were plotted in descending order. To study the correlation between CD274 gene and protein expression, pan-cancer transcriptomics and proteomics data were retrieved during the same period from the DepMap Portal (mRNA expression: log2 (TPM+1), 23Q2 Expression Public; relative protein expression: proteomics Q9NZQ7; https://depmap.org/portal/) [32]. Spearman's correlation analysis was applied to the entire pan-cancer cell line cohort (N = 375) and restricted to AML cell lines (N = 14).

To validate CD274 surface expression, the following AML cell lines were used: Erythroid FAB M6: OCI-M1, HEL, F36P, and TF-1; Megakaryoblastic FAB M7: M07E and SET2; Monocytic FAB M5: U937. Cell lines were seeded 24 h prior at a concentration of 3×10^5 cells/ML in fresh culture medium. After 24 h, 2×10^5 cells were washed with PBS and incubated for 20 min at room temperature (RT) in the dark with an anti-human CD274-APC antibody or an isotype control (Miltenyi Biotech; see Table S18 for details). After incubation, samples were resuspended in 200 μl of RPMI 1640 medium without phenol red and analyzed by flow cytometry (LSRFortessa™ X-20, BD Biosciences, Erembodegem, Belgium). Ten thousand events were recorded for each sample using BD FACSDiva™ software, and the data were analyzed with FlowJo v10 software (BD Biosciences).

2.6. Statistical analysis

Statistical analyses were performed using GraphPad Prism software (version 10.4.1, GraphPad), except for specific bioinformatics studies. Non-parametric ANOVA (Kruskal-Wallis test) was used to assess differences between FAB groups. The Mann-Whitney test was applied for pairwise comparisons to the overall mean. Statistical details, including the number of samples and experiments, are provided in the figure legends. Significance thresholds: *P*-values < 0.05 were considered significant. *P* values were denoted as: * < 0.05, ** < 0.01, *** < 0.001, **** < 0.0001. The association between MK/Ery or Mo/ML polygenic mean or CD274 expression (top/bottom quartiles) and clinical features was analyzed using Fisher's exact tests, following AML patient stratification. Spearman's correlations (two-sided) were applied where specified.

2.7. Ethical availability statement

This study retrospectively analyzes publicly available cohorts, including AML patients and healthy donors. The use of these data complies with the specified terms and conditions, and proper acknowledgment has been made. All data are anonymized in accordance with policies for public-use databases. No additional ethical statement is required.

3. Results

3.1. Megakaryocytic/erythroid signature identifies AML patients exhibiting a dysfunctional TIL-enriched TME and CD274 (PD-L1) overexpression

We generated an MK/Ery polygenic marker based on the expression of 13 genes associated with MK/Ery differentiation (Table S1) [18,25]. We trained it on the pediatric AML cohort available from the St. Jude Children's Research Hospital (PeCan portal, N = 305, https://pecan.stjude.cloud), which includes a substantial number of AML patients with MK/Ery maturation stage disease (Fig. S1A). Correlation studies confirmed a strong association between the MK/Ery marker and genes frequently overrepresented in MK/Ery differentiation, including BCL2L1 (Bcl-xL) [18]. AML cell lines recapitulated this expression pattern (Fig. S1B and Table S2).

Categorizing AML patients from various publicly available cohorts using the MK/Ery polygenic signature consistently revealed enrichment of inflammatory-related pathways, overexpression of pro-inflammatory cytokines, and an increased mutational burden in MK/Ery^{high} AML patients (Fig. 1**A-D**, Fig. S1C-**E**, Tables S3-S5). Because these alterations commonly occur during chronic antigen exposure, we hypothesized that MK/Ery^{high} AML patients would display increased T-cell infiltration and potentially exhibit immune dysfunction.

Bulk specimens largely capture gene expression of the tumor microenvironment (TME). We used xCell [24], a gene signature-based enrichment method that estimates the relative cell abundance of up to 64 immune and stromal cell types from bulk RNA-Seq gene expression data. As the xCell web tool provides precomputed enrichment scores for TCGA LAML and TARGET AML samples, we compared the cell type enrichment scores in the TME of MK/Ery^{high} vs. MK/Ery^{low} AML patients from these two cohorts.

In parallel, we investigated similarities between AML patient blasts and cell lines exhibiting erythroleukemic or megakaryoblastic differentiation. Using the erythroleukemia OCI-M1 cell line as a reference, we applied the Celligner algorithm to classify AML patients from the TCGA LAML and TARGET AML cohorts as either OCI-M1-proximal or OCI-M1-

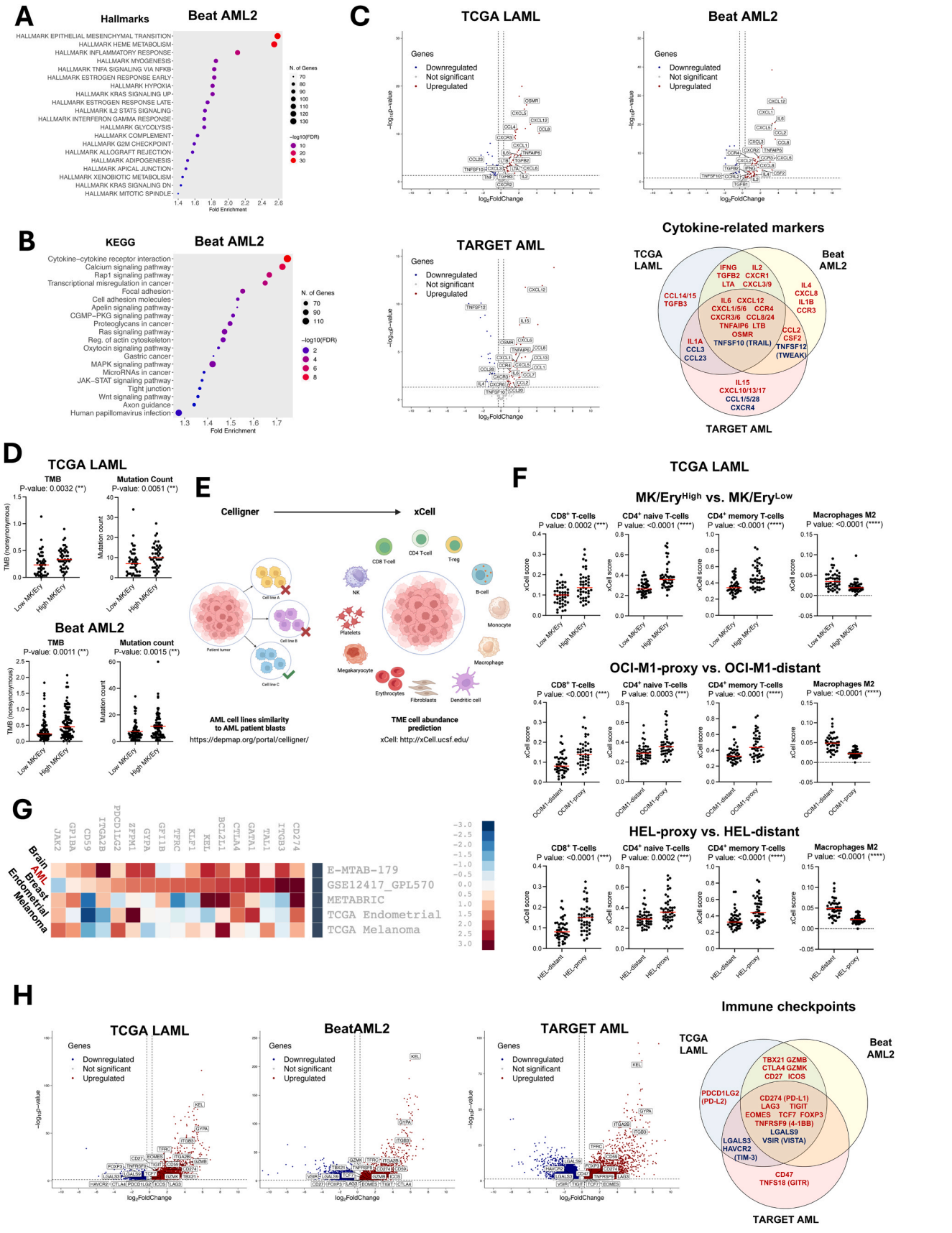

(caption on next page)

Fig. 1. MK/Ery^{High} AML Exhibit a Dysfunctional TIL-Enriched Tumor Microenvironment (TME). To predict TME alterations, AML specimens sampled from the bone marrow (BM) were selected from a cohort of non-redundant AML samples (see Materials and methods for sample filtering details; additional information is provided in Fig. S2A and Table S16). **(A)** Hallmark and **(B)** KEGG pathway enrichment analysis of differentially expressed genes in BM AML patients from the BM Beat AML2 cohort, categorized based on MK/Ery polygenic marker expression. Data processing and visualization were performed using ShinyGo 0.81, with significantly modulated genes selected for MK/Ery^{High} vs. MK/Ery^{Low} (top/bottom quartiles; log2 fold change threshold < -0.3 or > 0.3; FDR < 0.05). **(C)** Volcano plots depicting selected cytokine-related factors modulated in MK/Ery^{High} AML across publicly available datasets (BM Beat AML2, N = 325; TCGA LAML, N = 179; BM TARGET AML, N = 119). Differential gene expression (DGE) analysis was conducted in R, and overlapping modulated genes were visualized (red: significantly upregulated; blue: significantly downregulated; see Tables S3–S6). **(D)** Comparative analysis of tumor mutational burden and total mutational counts between MK/Ery^{High} and MK/Ery^{Low} groups in TCGA LAML and Beat AML2 cohorts (non-parametric Mann-Whitney *U* test, two-sided). **(E)** Schematic representation of the experimental strategy used to predict TME cell type abundance, combining Celligner and xCell algorithms to identify AML blasts with proximity to specific AML cell lines. **(F)** Selected TME cell types predicted to be modulated in the adult TCGA LAML cohort, stratified by MK/Ery expression or by proximity to the erythroleukemia cell lines OCI-M1 and HEL (non-parametric Mann-Whitney *U* test, two-sided; see Table S6 for extended analysis). **(G)** Plot retrieved from TIDE (http://tide.dfci.harvard.edu) ranking the T-cell dysfunction score associated with the queried gene list, with data ordered according to the AML cohorts included in the database (Metzeler; GSE12417). **(H)** Volcano plots illustrating selected immunosuppression-related factors modulated in MK/Ery^{High} AML, based on the same cohorts analyzed in (C), following DGE analysis in R (red: significantly upregulated; blue: significantly downregulated).

distant based on the Euclidean distance (ED) between the UMAP coordinates of OCI-M1 and those of the TCGA LAML or TARGET AML specimens (see Material and Methods, paragraph 2.3) [27]. We then compared the cell type enrichment scores between OCI-M1-proxy (low ED values) and OCI-M1-distant (high ED values) AML groups using xCell (Fig. 1**E**) [24]. To confirm consistent data alignment with AML patient samples, we repeated the same analysis using the erythroleukemia HEL cell line. Both MK/Ery^{high} AML, OCI-M1-proxy, and HEL-proxy AML groups exhibited a significantly higher predicted abundance of CD8$^+$ T-cells, CD4$^+$ naïve T-cells, and CD4$^+$ memory T-cells, along with a marked depletion of monocytes, M2 macrophages, natural killer T-cells (NKTs), and Pro-B-cells; these results were consistent in the adult TCGA LAML and the pediatric TARGET AML samples (Fig. 1**F**, Fig. S1F, and Table S6).

The TIDE algorithm [28] assigned a significantly higher T-cell dysfunctional score to the MK/Ery gene list (Fig. 1**G**). Consistent with this prediction, bulk RNA-Seq differential gene expression (DGE) analysis confirmed the upregulation of immune checkpoints (ICs) and factors involved in T-cell activation, exhaustion, and differentiation across all cohorts examined (Fig. 1**H**). These results suggest that the MK/Ery phenotype is characterized by bone marrow (BM) infiltration of a broad spectrum of T-cell phenotypes, ranging from naïve to cytotoxic. This continuum features an overrepresentation of markers associated with stem-like, exhausted, and memory T-cells, indicating a possible immune escape mechanism.

A notable association emerged between the MK/Ery signature and CD274 (Programmed Death Ligand (PD-L)1) gene expression. This was observed in AML blasts from BM aspirates, peripheral blood (PB), and leukapheresis (LK) specimens (Fig. S2A). It remained consistent across all adult and pediatric AML cohorts and aligned with the FAB (French-American-British) classification (Fig. 2**A-B** and, Fig. S2B-S2C). Moreover, patients diagnosed with myelodysplastic syndrome (MDS) (including current diagnosis or antecedent to AML) and those exhibiting myelodysplastic-related changes (MRC-AML), harboring TP53 mutations or predicted to have stem-like blasts consistently displayed a CD274^{high} phenotype, aligning with the MK/Ery phenotype categorization (Fig. 2**C**, Fig. S2D-**E**, and Tables S7-S8).

AML cell lines mirrored these patient blast characteristics. Among the top CD274-expressing lines were the erythroid (FAB M6) OCI-M1, HEL, F36P, and the megakaryoblastic (FAB M7) M07E and SET2 cell lines (https://depmap.org/portal/). AML cells of MDS origin likewise demonstrated the CD274^{high} phenotype. Consistent with patient data, the MK/Ery gene signature strongly correlated with CD274 and BCL2L1 expression in the cell line cohort (Fig. 2**D-E** and Fig. S2F-**G**). CD274 mRNA expression (log2(TPM+1); 23Q2 Public) correlated well with relative CD274 protein levels (proteomics; Q9NZQ7; https://depmap.org/portal/) [32], both in pan-cancer (N = 375) and AML cell line-restricted analyses (N = 14) (Fig. 2**F**). In agreement with RNA-Seq and proteomics data, OCI-M1, HEL, and F36P displayed the highest CD274 surface levels by flow cytometry, whereas M6 TF-1 cells were confirmed to be CD274-negative (Fig. 2**G**). Overall, CD274 expression trends remained consistent between mRNA/protein and membrane localization analyses.

Given the similarity between AML cell lines and MK/Ery AML blasts, we hypothesized that the CD274 signal detected in bulk RNA-Seq data for MK/Ery^{high} AML patient BM aspirates originates from the blast population. To confirm, we used single-cell RNA-Seq data from MK/Ery AML patient samples recently investigated by Kuusanmaki and colleagues [18] (Fig. 2**H**). Analysis of a BM specimen (termed AML-5) from a patient who progressed from essential thrombocythemia to erythroid AML revealed multiple large erythroid clusters exhibiting varying differentiation states based on the CD34/CD71/GlyA triad. The CD34-CD71$^+$GlyA$^+$ cluster displayed a significant CD274 upregulation. In the second specimen (AML-1) from a patient who progressed from MDS to megakaryocytic AML, numerous megakaryocytic/erythroid-like clusters were detected. Notably, the CD34$^+$CD71$^+$GlyA$^-$ cluster had the highest CD274 upregulation among all identified subpopulations (Fig. 2**H**). These findings confirm that CD274 overexpression arises within specific malignant subclones, implying distinct roles for the co-existing MK/Ery AML subpopulations.

Both patient samples had a substantial lymphoid fraction, accounting for 37 % and 82 % of the non-megakaryocytic/erythroid population, respectively, with CD8$^+$ T-cells comprising ~14 % and 27 % (Table S9). Assessing eight BM specimens from the Human Cell Atlas (HCA) consortium revealed that the lymphoid cell fraction (CD8$^+$ T-cells and naïve CD8$^+$ T-cells) averaged 30 % (range: 15–42 %), increasing progressively with age (Table S10).

These findings illustrate that AML with megakaryocytic/erythroid features is characterized by a T-cell–rich yet dysfunctional immune environment, driven partly by high CD274 (PD-L1) expression. Building on these observations, we next examined whether other AML subtypes, particularly those with myelomonocytic/monocytic differentiation, display distinct immunomodulatory profiles.

3.2. Diversified immune marker expression and T-cell-depleted TME characterize AML patients with myelomonocytic/monocytic differentiation status

AML clones with monocytic differentiation have immunomodulatory functions. Van Galen and colleagues described immunosuppressive activity in monocytic subclones [1], and Yeaton and collaborators reported inflammatory mechanisms driven by aberrant monocytes progressing into leukemic forms [2].

We generated a polygenic marker to identify ML/Mo AML subtypes using the 16-gene list from our previous study [7] (Table S1). Categorizing AML patients from multiple publicly available cohorts validated the pro-inflammatory nature of the ML/Mo^{High} phenotype. Gene Set Enrichment analyses (GSEA) indicated that interleukin/STAT (signal transducer and activator of transcription) pathways were exacerbated in both adult and pediatric cohorts. Adult ML/Mo^{High} patients also showed

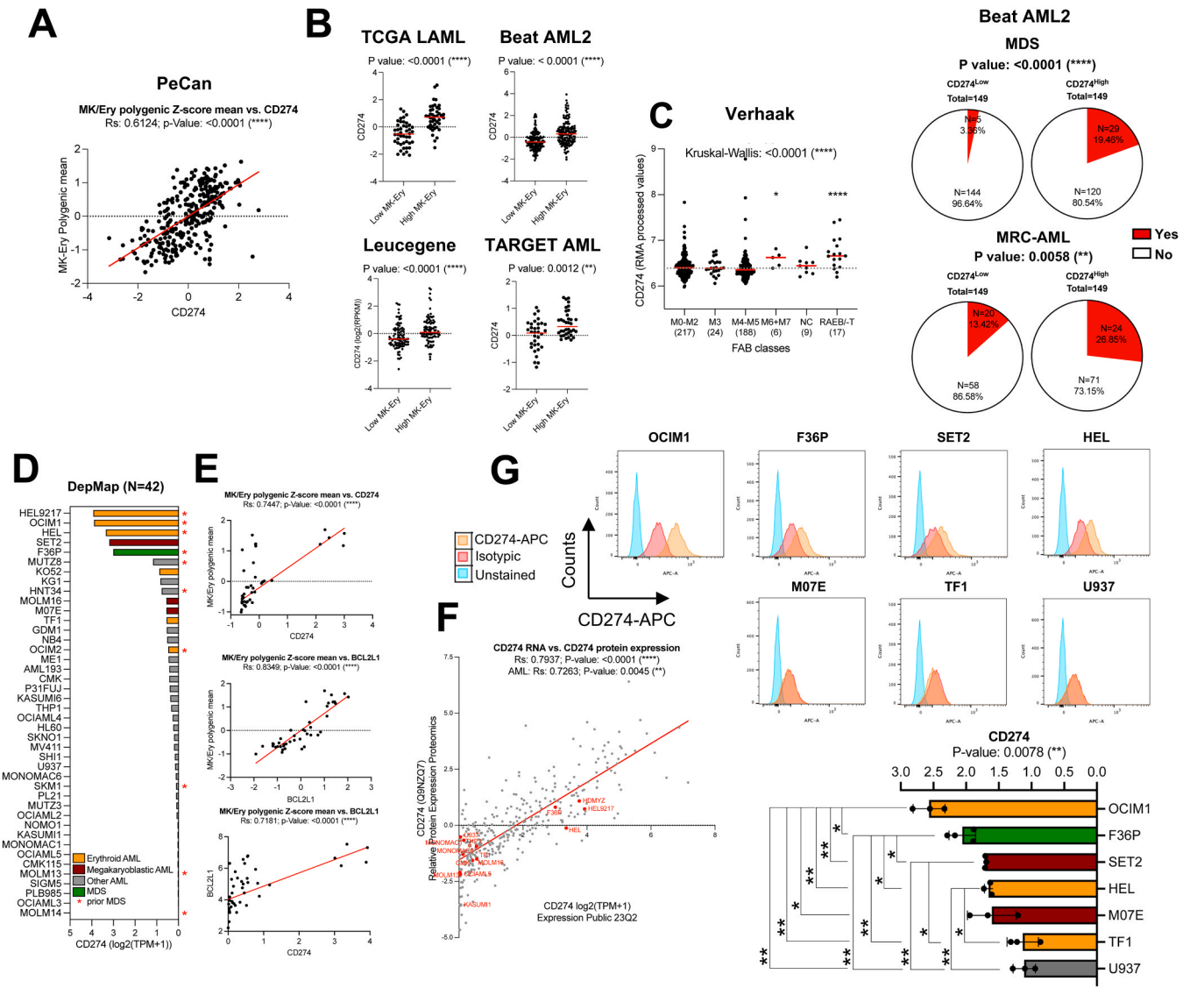

(caption on next page)

Fig. 2. MK/Ery^{High} AML Overexpress CD274 (PD-L1). **(A)** The PeCan pediatric AML cohort from St. Jude Children's Research Hospital (https://pecan.stjude.cloud) was used to train the 13-gene MK/Ery polygenic marker (N = 305, including N = 89 megakaryoblastic AML patients). A significant positive correlation was observed between MK/Ery signature expression and *CD274* gene expression (Z-score values; Spearman's correlation, Rs; two-sided). **(B)** *CD274* expression levels in publicly available AML cohorts (Beat AML2, TCGA LAML, Leucegene, and TARGET AML) were stratified by MK/Ery phenotype (non-parametric Mann-Whitney *U* test, two-sided). **(C)** Association between CD274 expression and myelodysplastic syndromes (MDS). CD274 expression was analyzed in the Verhaak cohort (GSE6891), stratified by FAB classification, including N = 17 MDS patients (Kruskal-Wallis test, p-value < 0.0001; non-parametric Mann-Whitney *U* test, two-tailed for pairwise comparisons to the overall median; p-values < 0.05). Right panels: Fisher's exact test (two-sided) applied to the Beat AML2 cohort demonstrated a significantly higher proportion of AML patients with a prior MDS diagnosis or myelodysplastic-related changes (MRC) in the CD274^{High} patient group (top/bottom quartiles; p-value < 0.01; see Tables S6–S7). **(D)** CD274 mRNA expression in 42 AML cell lines retrieved from the DepMap Project. **(E)** Correlation analysis between the MK/Ery polygenic marker and CD274 and/or BCL2L1 expression in the same AML cell line panel (Spearman's correlation, Rs; two-sided). **(F)** Correlation of CD274 mRNA expression with CD274 protein expression across all cancer cell lines (N = 375) and AML-restricted cell lines (N = 14) in the DepMap dataset (Spearman's correlation, Rs; two-sided). **(G)** Flow cytometric analysis of CD274 surface expression in selected AML cell lines, including M6/M7 and MDS-derived models (One-way ANOVA; at least N = 3 independent experiments). **(H)** Uniform Manifold Approximation and Projection (UMAP) plot of scRNA-seq data from AML patients with erythroid (AML-5) or megakaryoblastic (AML-1) differentiation, showing clustering based on SingleR cell annotation. Expression levels of selected modulated genes are reported for specific malignant subpopulations (see Table S9 and Fig. S2H).

enriched responses to interferon-α/γ and TNFα (tumor necrosis factor) signaling via the NF-κB (nuclear factor-kB) pathway (Fig. 3**A** and Fig. S3A). Differential gene expression (DGE) analysis confirmed the upregulation of various cytokines and chemokines, including several linked to the TNFα and TGF-β pathways (Fig. 3**B**, Fig. S3B-**C**, and Tables S11-S13).

Additionally, HLA (human antigen leukocyte) system I/II expression and immunosuppression-related factors (*LGALS3*, *LGALS9*, *VSIR*, *ENTPD1*, and *HAVCR2*) were significantly increased (except for *HAVCR2*, which remained unchanged in the pediatric cohort); inconsistent changes were observed across categorizations of all selected cohorts for *CD274*, *LAG3*, *CTLA4*, *TBX21*, and *EOMES,* while *TOX, TNFSF4 (OX40L)* and *CD47* were downregulated (Fig. 3**C-D**, Fig. S3D, and Tables S11-S14). This expression pattern was reproduced by categorizing the same cohorts into MONO-MAC-1-proxy vs. MONO-MAC-1-distant groups using Celligner (Fig. 3**C** and Fig. S3C). The prediction of a more differentiated AML phenotype further confirmed the robustness of our polygenic marker (Fig. 3**E** and Fig. S3E).

When AML patient samples were categorized by ML/Mo signature or similarity to MAC-1-proxy (using the same methodology described for MK/Ery AML), a reduced lymphoid infiltration emerged consistently in both adult TCGA LAML and pediatric TARGET AML cohorts. Several T-cell subsets (naïve CD8$^+$/CD4$^+$, CD8$^+$ central memory T-cells, CD4$^+$ memory T-cells, and T regulatory cells) were diminished (Mann-Whitney test, two-tailed, p-values < 0.05; Fig. 3**F**, Fig. S3F, and Table S15). In contrast, M2 macrophages and dendritic cells were overrepresented, whereas ML/Mo^{High} patients showed a lower tumor mutational burden (Fig. S3G).

These data predict a T-cell-depleted ("cold") and TAM (tumor-associated macrophage)-enriched TME in ML/Mo^{High} AML. By contrast, MK/Ery^{High} AML features a highly infiltrated ("hot") TME. Despite the distinct immunomodulatory profiles of these differentiation-associated polygenic markers, AML blasts linked to each are expected to be immune-inhibitory. We, therefore, sought to experimentally validate their immune-suppressive properties through in vitro co-culture models.

3.3. In vitro T-cell and AML cell line co-culture assay confirms the immune-suppressive phenotype of MK/Ery and ML/Mo subgroups found in patients

To validate the immune-suppressive roles suggested by our transcriptomic and computational findings, we conducted a series of in vitro co-culture assays. Specifically, we tested how representative MK/Ery- and ML/Mo-like AML cell lines affect CD8$^+$ T-cell proliferation and activation under controlled conditions.

We designed an experimental strategy combining T-cell and AML cell line co-cultures, followed by sequential flow cytometry gating (Fig. 4**A**). We monitored CD8$^+$ T-cell activation and proliferation under CD3/CD28 stimulation for 72 h by examining cell frequencies in successive generations (see methods).

Among MK/Ery cell lines, the percentage of T-cells in early generations was significantly higher in cultures without AML cells than in co-cultures with OCI-M1, HEL, and F36P (p-values < 0.05; Fig. 4**B**), indicating that these cell lines suppress T-cell proliferation. In contrast, M07E, SET2, and TF1 did not substantially affect T-cell proliferation (Mann-Whitney test, two-tailed, p-values > 0.05).

A similar analysis was performed on ML/Mo-like AML cell lines. MUTZ3, MONO-MAC-1, and MONO-MAC-6 significantly inhibited T-cell proliferation in at least three of four T-cell generations (two-tailed T-test, p-values < 0.05), and T-cells co-cultured with THP1 had lower percentages in generations 1 and 3 compared to T-cells alone. The U937 (M5) cell line showed no statistically significant reduction (two-tailed T-test, p-values > 0.05). Lastly, the M2 cell line HL60 had minimal effects on T-cell proliferation (Fig. 4**B-C**).

We applied multiple computational methods to quantify the magnitude of AML-induced inhibition (methods). The complement-to-division index ratio (CDR) estimates inhibition of the average number of cell divisions across all T-cells initially seeded for co-culture. The complement-to-expansion index ratio (CER) captures the reduction in fold expansion of T-cells during culture. Lastly, the complement-to-proliferation index ratio (CPR) measures the inhibition of the average number of divisions among responding T-cells. We also calculated the ratio of the percentage of T-cells in the first two generations (co-culture vs. culture alone) to assess delayed proliferation. A non-parametric Kruskal-Wallis test showed significant differences among cell lines (p-values < 0.0001, Fig. 4**D**).

HEL and OCI-M1 significantly inhibited T-cell proliferation (72-hour timepoint) based on CER (Mann-Whitney test, two-sided, HEL: p-value = 0.0349, OCI-M1: p-value = 0.0326). Although F36P did not reach statistical significance, it showed a mild but consistent inhibitory trend across all metrics. M07E and SET2 had no measurable inhibitory effects (Mann-Whitney test, two-sided, p-values > 0.05), whereas TF1 appeared to enhance T-cell proliferation, but without statistical significance (Mann-Whitney test, two-sided, p-values > 0.05; Fig. 4**D**).

Likewise, the myelomonocytic MUTZ-3 cell line significantly inhibited T-cell proliferation, demonstrated by CER and CDR (Mann-Whitney test, two-tailed, CER: p-value = 0.0041, CDR: p-value = 0.0062; Fig. 4**D**). MONO-MAC-1 also remained above the overall median in most inhibitory metrics. By contrast, the U937 (M5) cell line consistently increased T-cell proliferation (similar to TF1) across all indicators (Mann-Whitney test, two-sided, p-values < 0.001, Fig. 4**D**). As expected, the M2 HL-60 line did not affect T-cell proliferation.

These data indicate that MK/Ery and ML/Mo AML cell models can exert inhibitory effects on CD8$^+$ T-cells. The degree of inhibition by MK/Ery AML cells correlated with their PD-L1 surface expression, except for SET2, suggesting the involvement of additional, unidentified mechanisms in T-cell interactions.

Co-culture of CFSE-labeled primary T-cells with HEL cells for 72 h led to a pronounced reduction in CFSE dilution, indicating effective suppression of T-cell proliferation (Fig. 4**B**). Preliminary dose-finding in

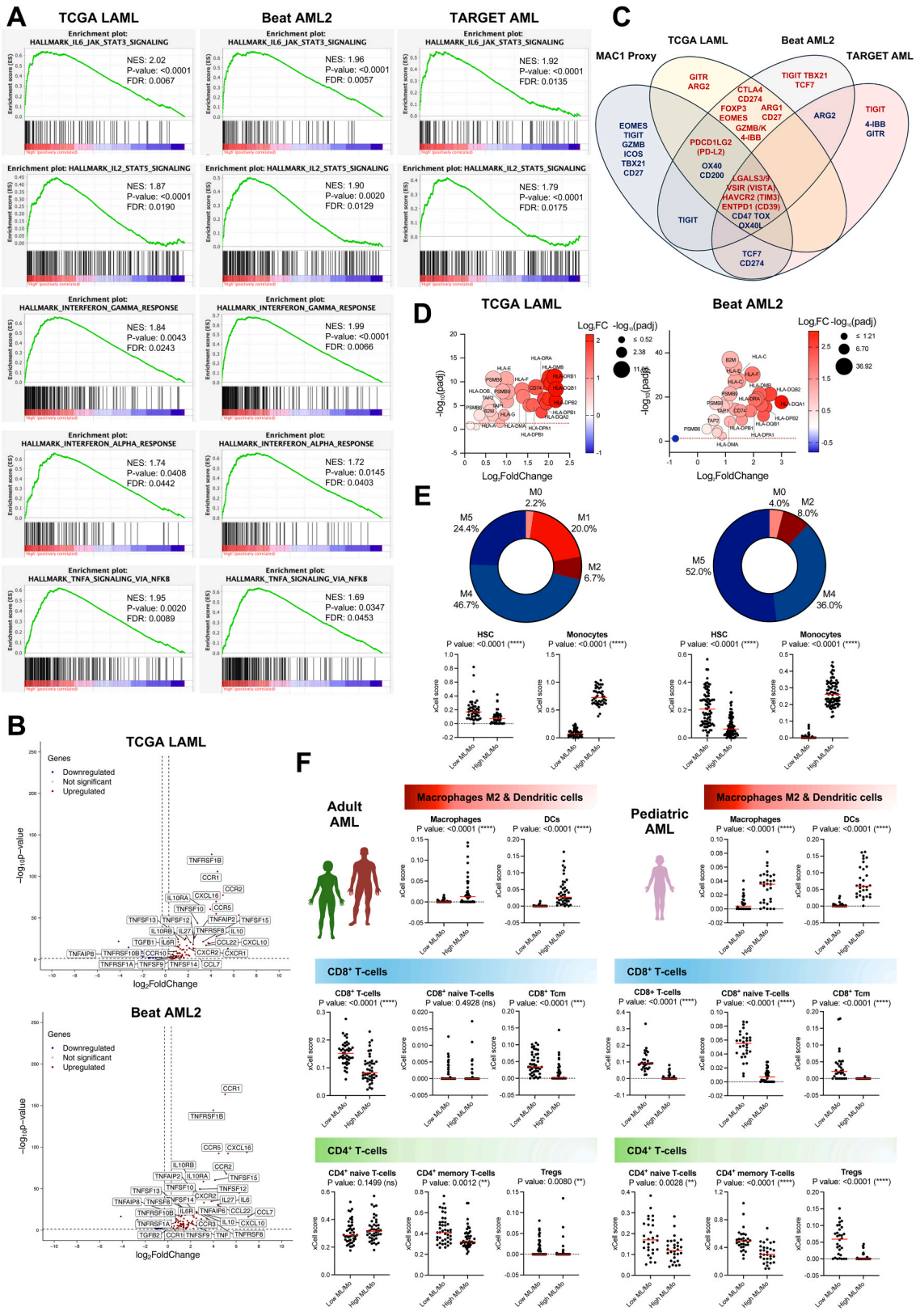

Fig. 3. Immune Marker Expression and T-Cell–Depleted TME in ML/Mo AML. **(A)** GSEA plot showing significant enrichment (FDR < 0.05) of differentially expressed genes across Hallmark molecular signatures in AML patients from TCGA LAML, BM Beat AML2, and BM TARGET AML cohorts, categorized by ML/Mo polygenic signature expression (Table S1). **(B)** Volcano plots illustrating selected cytokine-related factors modulated in ML/Mo^{High} AML. **(C)** Common and distinct immune checkpoint-related genes visualized in a Venn diagram (Tables S11–S13). **(D-E)** HLA-I/II gene expression modulation and its association with AML blast maturation stage, analyzed in TCGA LAML and Beat AML2 cohorts, categorized by FAB classification (top panel: Kruskal-Wallis test, $p < 0.0001$) and HSC or committed monocytic differentiation using xCell (non-parametric Mann-Whitney *U* test). **(F-G)** Selected TME cell types predicted to be modulated in TCGA LAML and BM TARGET AML cohorts, categorized by ML/Mo expression (non-parametric Mann-Whitney *U* test, two-sided; see Table S14 for extended analysis).

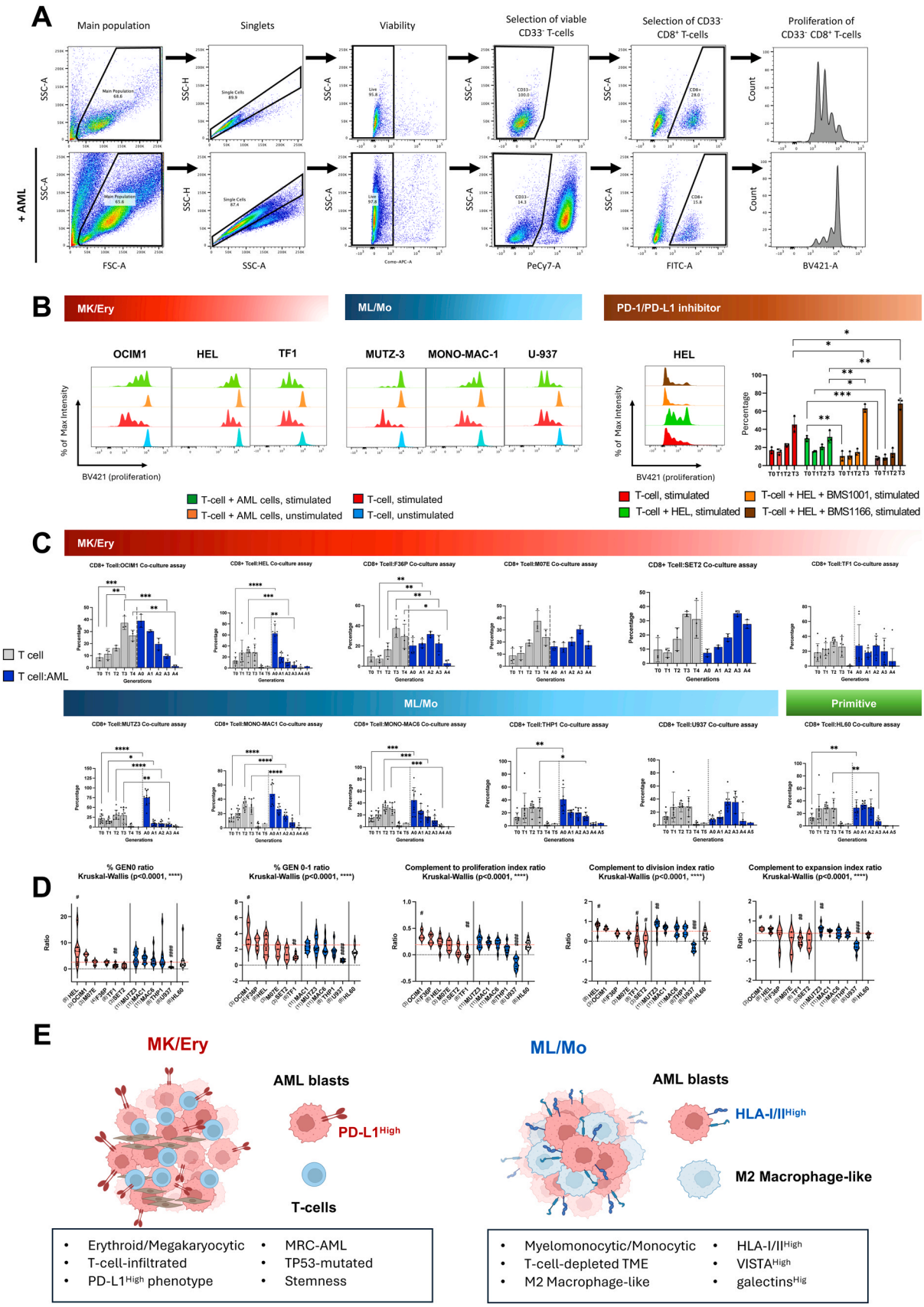

(caption on next page)

Fig. 4. Experimental Validation of T-Cell Modulatory Activity in AML Cells. **(A)** Multiparametric flow cytometry gating strategy for monitoring T-cell proliferation and immune factor expression. **(B)** Proliferation profiles of T-cells after 72 h of stimulation, with or without co-culture with AML cell lines. Small-molecule PD-1/PD-L1 inhibitors enhance $CD8^+$ T-cell proliferation inhibited by HEL cells. T cells were cultured alone, co-cultured with HEL cells, or co-cultured with HEL cells in the presence of BMS-1166 (1.2 μM) or BMS-1001 (1.2 μM) for 72 h. Quantification of T-cell generation percentages derived from CFSE dilution. Bars represent mean ± SD of three biological replicates. BMS-1166 and BMS-1001 increased proliferation by 2.2-fold and 2.0-fold, respectively, compared to vehicle control (T-test, two-sided, p-values < 0.05). **(C)** Effect of AML cell lines on T-cell generation percentages, comparing T-cells cultured alone vs. in co-culture with AML cells (T-test, two-sided, p-values < 0.05). Gray bars represent T-cells cultured alone, while blue bars represent T-cells co-cultured with AML cells. **(D)** Quantification of $CD8^+$ T-cell proliferation inhibition over 72 h, assessed using different indices: Generation 0 or 0 + 1 ratio, complement-to-division index ratio (CDR), complement-to-expansion index ratio (CER), complement-to-proliferation index ratio (CPR). Data are ordered by decreasing inhibitory potential, categorized by AML subtype: red boxes indicate MK/Ery AML cell lines (HEL, OCI-M1, SET2, F36P, M07E, TF1), blue boxes indicate ML/Mo AML cell lines (MUTZ3, MONO-MAC-1, MONO-MAC-6, THP1, U937), and the white box represents the M2 control cell line (HL60). Statistically significant differences were observed among AML cell lines (Kruskal-Wallis test, two-sided, p-value < 0.0001) and in comparisons with the overall median (Mann-Whitney test, two-sided; HEL: p-value $= 0.05$). **(E)** Association between MK/Ery and ML/Mo markers and clinical features in a proposed model.

HEL and Jurkat T-cell mono and co-cultures confirmed that the working concentrations of BMS-1166 and BMS-1001 did not compromise cell viability, thereby ruling out off-target cytotoxicity (Fig. S4). Pharmacological inhibition of the PD-1/PD-L1 axis with either BMS-1166 (1.2 μM) or BMS-1001 (1.2 μM) restored proliferative capacity. At the working concentrations, $CD8^+$ T-cell proliferation indices increased by 2.2- and 2.0-fold, respectively, compared with vehicle-treated co-cultures (Fig. 4**B**), confirming partial blockade of HEL-expressed PD-L1. Of note, BMS compounds further enhanced T-cell proliferation in co-culture settings compared to stimulated T-cells cultured alone. Under these conditions, no significant cytotoxicity was observed in primary T-cells or HEL cells. Thus, small-molecule PD-1/PD-L1 inhibitors effectively counteract HEL-mediated proliferative arrest, underscoring their potential to modulate antigen-specific T-cell responses in vitro.

4. Discussion

The immune landscape of AML extends beyond a simple "hot vs. cold" framework, emphasizing the need for more nuanced characterizations of the TME [33]. At one end of the spectrum, AML cases with robust T-cell infiltration yet evident immune dysfunction, exemplified by MK/Ery^{high} phenotypes, exhibit high levels of PD-L1 and other immune checkpoint molecules. This suggests that while T cells are present, they may be chronically challenged, often progressing toward intermediate states of exhaustion within a continuum of cell states [4]. This subclass is further associated with a propensity for stem-like or myelodysplastic-related genomic alterations, such as TP53 mutations, highlighting a complex interplay between lineage differentiation and immune escape (Fig. 4**E**).

As expected, all AML patients classified under the FAB morphology-based system as erythroid (M6) and megakaryocytic (M7) fall into the MK/Ery^{high} phenotype. The FAB M6/M7 subgroup represents a relatively small proportion of AML cases (M6: 3–5 %; M7: 7.5 % in adult AML, increasing to 24 % in pediatric cases). However, our MK/Ery marker captures a broader set of cases resembling the erythroid/megakaryocytic phenotypes identified by conventional diagnostic approaches.

Previous studies have highlighted the association between TP53-mutated MDS and AML and immune checkpoint inhibitors (ICIs), including PD-L1 [34]. Moreover, MDS patients frequently upregulate PD-L1 in response to hypomethylating agent-based treatments [35]. Additionally, the ELN 2022 classification has progressively refined the relevance of MDS/MRC as a predisposing feature in AML diagnosis [36]. Altogether, this evidence suggests that the MK/Ery^{High} phenotype is more than a surrogate marker of blast differentiation; rather, it may define a distinct AML subgroup consistently characterized by enriched clinical features and alterations, including higher *CD274* (PD-L1) expression and tumor-infiltrating lymphocytes (TILs). This observation has two important implications. First, as AML undergoes dynamic clonal evolution and blast dedifferentiation, this phenotype may emerge secondarily due to therapy-induced selection pressures as a resistance strategy [19]. Second, the enrichment of MK/Ery-associated gene signatures may extend beyond AML to other tumor types, including solid malignancies. Notably, a significant proportion of tumor-infiltrating myeloid cells originate from erythroid precursors, and their trans-differentiation enhances TME immunosuppressive effects, ultimately reducing the efficacy of anti-PD-1/PD-L1 therapies [37].

Our findings support the increasing evidence that small-molecule PD-L1 antagonists can effectively replace therapeutic antibodies in abrogating checkpoint-mediated T-cell suppression. Both BMS-1166 and BMS-1001 bind to PD-L1 with nanomolar affinity, creating hydrophobic dimer interfaces that sterically hinder PD-1 engagement and initiate ligand internalization [5]. In the HEL co-culture system, this resulted in a significant recovery of $CD8^+$ T-cell proliferation, mirroring the effectiveness of antibody blockade, yet achieved with compounds that are approximately 100-fold smaller and suitable for intracellular or intratumoral penetration. Notably, BMS compounds further exacerbate T-cell proliferation in co-culture settings. Considering the predicted high TMB and increased T-cell infiltration in MK/Ery AML patients (Fig. 1 and Fig. S1), these findings further support our hypothesis that IC overexpression in this subgroup represents a key mechanism of immune evasion.

From a translational perspective, small molecules offer several practical advantages: (i) oral bioavailability and adjustable pharmacokinetics, allowing flexible dosing schedules; (ii) reduced manufacturing complexity and cost compared to biologics; and (iii) improved tissue distribution, which may overcome the limited stromal penetration seen with bulky IgG antibodies. Additionally, chemical checkpoint inhibitors can be co-formulated with existing targeted therapies or chemotherapeutics to create fixed-dose combinations, in line with precision immuno-oncology strategies. Nonetheless, off-target liabilities, metabolic stability, and the possibility of systemic immune-related adverse events require further optimization. In the future, we will explore whether BMS-series compounds synergize with ICD-inducing chemotherapies or metabolic modulators in myeloid leukemia models, and whether their efficacy extends to primary AML blasts with intrinsic PD-L1 up-regulation.

AML cases characterized by myelomonocytic/monocytic differentiation (ML/Mo^{high}) frequently exhibit reduced T-cell infiltration but are dominated by immunosuppressive myeloid populations, including M2 macrophages, which rely on cytokine-rich yet inhibitory pathways. Notably, while ML/Mo^{high} tumors may express higher levels of MHC subunits, T-cell cytotoxicity remains limited, likely due to increased expression of immunosuppressive signals (e.g., VISTA, galectins, TIM-3) and an overall lack of robust T-cell presence (Fig. 4**E**). These findings align with previous reports that identify monocytic subclones as key mediators of intratumoral immunosuppression [1]. Similarly, our study supports the inhibitory effect of monocytic AML cell lines and markers. Our bulk transcriptomic analysis of the ML/Mo marker consistently shows enrichment in pro-inflammatory pathways, similar to those associated with aberrant monocytic populations expressing high MHC-II levels, which have been implicated in AML progression [2].

Between these two phenotypic extremes, a continuum of intermediate immune landscapes likely exists in which AML cases display

overlapping traits that evolve over time. This heterogeneity underscores the need for personalized therapeutic strategies.

For example, while we did not find a direct association between the MK/Ery^{High} phenotype and overall survival (OS), ongoing investigations in our laboratory indicate that combining CD274 (PD-L1) expression with additional immunosuppressive markers upregulated in this phenotype reveals a clear trend toward worse late-stage OS (not shown). Similarly, previous clinical trials in MDS cohorts have failed to demonstrate a survival benefit from anti-PD-L1 therapy [35,38], limiting its clinical advancement, which raises the question of whether combined ICIs could prevent AML blasts from using alternative routes of immunosuppression in these cases.

Recent studies emphasize the importance of topographical mapping of TME components and their functional states. Integrative multi-omics approaches—including transcriptomics, genomics, and proteomics—offer powerful tools for dissecting TME heterogeneity and elucidating the interplay between AML blasts and immune cells. Spatial omics techniques can provide critical insights into immune cell-blast interactions within the bone marrow architecture, revealing new targets for combination therapies.

Overall, our refined classification—ranging from T–cell–rich yet dysfunctional niches to T–cell–depleted, myeloid-driven environments—demonstrates the inadequacy of classifying AML as uniformly "cold." Recognizing this broader spectrum of TME states will enable the development of more precisely tailored immunotherapeutic strategies, incorporating checkpoint blockade, T-cell engagers, or macrophage reprogramming based on the immune composition of each patient's AML.

In AML, a fundamental challenge emerges because the cells typically used to delineate TME phenotypes in solid tumors and macrophages are malignant blasts with aberrant myeloid features [39]. First, these malignant cells often fail to fit the canonical M1/M2 polarization model, as they can secrete immunosuppressive cytokines or display M2-like markers while retaining partial or arrested differentiation programs. Second, AML blasts frequently co-opt immune functions, including checkpoint expression (e.g., PD-L1, VISTA) or myeloid-derived suppressor cell (MDSC)-like activity, obscuring the usual distinctions between tumor and immune compartments. This transformation is further amplified by an altered cytokine milieu (e.g., high TNF, IL-1β), which drives T-cell dysfunction and recruits tolerogenic non-transformed myeloid subsets, necessitating an integrative approach that acknowledges leukemic reprogramming of the myeloid niche rather than relying solely on T-cell- and/or M1/M2-centric classifications. Finally, therapeutic success in AML may depend on recognizing this blurred boundary between physiological macrophages and malignant myeloid blasts. Ultimately, refined classifications tailored specifically to AML's pathology, particularly distinguishing MK/Ery^{high} from ML/Mo^{high} disease, will better inform prognostic assessments and identify rational combination therapies.

5. Conclusion

Future spatial multi-omics investigations, including spatial transcriptomics, imaging mass cytometry, and multiplex immunohistochemistry, will be critical for visualizing the topological distribution of these immune cell states within the bone marrow. These advanced tools will enable precise mapping of AML immune niches, facilitate the identification of actionable vulnerabilities, and ultimately guide the development of more targeted immunotherapeutic strategies.

Our refined classification highlights the diverse immune contexts of AML, from T-cell–rich yet dysfunctional niches in MK/Ery^{high} AML to highly myeloid-infiltrated, T-cell–depleted environments in ML/Mo^{high} AML. These insights underscore the inadequacy of classifying AML as universally "cold," advocating for tailored immunotherapeutic strategies based on each patient's immune phenotype. Moving forward, spatial multi-omics approaches will be instrumental in resolving intratumoral heterogeneity, allowing for the development of combination therapies that simultaneously address T-cell dysfunction, myeloid-derived immunosuppression, and blast-intrinsic escape mechanisms. Our data also establish that pharmacological PD-L1 blockade with the small-molecule inhibitors BMS-1166 and BMS-1001 effectively reverses HEL-mediated T-cell suppression, restoring CD8^{+} T-cell proliferation. These results highlight the promise of immunotherapeutic strategies in defined myeloid leukemia subsets, such as erythroid/megakaryocytic-like AML, which are traditionally considered refractory to immune-based interventions. The efficacy of compact, orally deliverable checkpoint inhibitors positions them as versatile components of future combination regimens in myeloid leukemia immunotherapy.

CRediT authorship contribution statement

Claudia Cerella: Writing – review & editing, Writing – original draft, Visualization, Validation, Supervision, Software, Project administration, Methodology, Investigation, Funding acquisition, Formal analysis, Data curation, Conceptualization. **Marc Diederich:** Writing – review & editing, Writing – original draft, Validation, Supervision, Software, Resources, Project administration, Methodology, Investigation, Funding acquisition, Formal analysis, Data curation. **Yejin Lee:** Formal analysis, Investigation, Methodology, Visualization. **Ji Yeon Paik:** Formal analysis, Investigation, Methodology, Visualization. **Correia Da Cruz Leslie:** Visualization, Software, Methodology, Investigation. **Jeonghye Park:** Formal analysis, Investigation, Methodology, Visualization.

Ethics approval

All publicly available datasets were analyzed according to their respective usage terms (see methods and Table S16). PBMCs from healthy donors were obtained from the Luxembourg Red Cross (Luxembourg) upon donors' consent and approval from the Luxembourg Red Cross Ethical Committee (Authorization Numbers: LBMCC-2019–0001; LBMCC-2019–0002).

Funding

LBMCC: "Recherche Cancer et Sang" foundation, the "Een Häerz fir kriibskrank Kanner", the Action LIONS "Vaincre le Cancer" and Télévie Luxembourg. A doctoral Télévie grant supported LC. CC acknowledges support from the "Fondation Gustave et Simone Prévot" (Geneva, Switzerland). SNU: the "Recherches Scientifiques Luxembourg" association, the National Research Foundation (NRF) [Grant Number 370C-20220063]; MEST of Korea for Tumor Microenvironment Global Core Research Center (GCRC) [Grant Number 2011-0030001]; Brain Korea (BK21) FOUR program and Creative-Pioneering Researchers Program at Seoul National University [Funding number: 370C-20250066].

Declaration of Generative AI and AI-assisted technologies in the writing process

During the preparation of this work, the author(s) used Grammarly.com and ChatGTP to improve language and readability. After using this tool/service, the author(s) reviewed and edited the content as needed and took full responsibility for the publication's content.

Declaration of Competing Interest

The authors declare that they have no known competing financial interests or personal relationships that could have appeared to influence the work reported in this paper.

Acknowledgments

Artwork was created in BioRender. Correia, L., Cerella, C. and Diederich, M. (2025) https://BioRender.com/t76g667

Appendix A. Supporting information

Supplementary data associated with this article can be found in the online version at doi:10.1016/j.biopha.2025.118287.

Data availability statement

All patient cohorts analyzed in this study are from publicly available cohorts; their data are available through their corresponding websites, as detailed in supplemental methods and Table S16. All the other data are available upon request to the authors.

References

[1] P. van Galen, V. Hovestadt, M.H. Wadsworth Ii, T.K. Hughes, G.K. Griffin, S. Battaglia, J.A. Verga, J. Stephansky, T.J. Pastika, J. Lombardi Story, G.S. Pinkus, O. Pozdnyakova, I. Galinsky, R.M. Stone, T.A. Graubert, A.K. Shalek, J.C. Aster, A. A. Lane, B.E. Bernstein, Single-cell RNA-seq reveals AML hierarchies relevant to disease progression and immunity, Cell 176 (6) (2019) 1265–1281, e24.

[2] A. Yeaton, G. Cayanan, S. Loghavi, I. Dolgalev, E.M. Leddin, C.E. Loo, H. Torabifard, D. Nicolet, J. Wang, K. Corrigan, V. Paraskevopoulou, D. T. Starczynowski, E. Wang, O. Abdel-Wahab, A.D. Viny, R.M. Stone, J.C. Byrd, O. A. Guryanova, R.M. Kohli, G.A. Cisneros, A. Tsirigos, A.K. Eisfeld, I. Aifantis, M. Guillamot, The impact of inflammation-induced tumor plasticity during myeloid transformation, Cancer Discov. 12 (10) (2022) 2392–2413.

[3] F.M. Uhl, S. Chen, D. O'Sullivan, J. Edwards-Hicks, G. Richter, E. Haring, G. Andrieux, S. Halbach, P. Apostolova, J. Buscher, S. Duquesne, W. Melchinger, B. Sauer, K. Shoumariyeh, A. Schmitt-Graeff, M. Kreutz, M. Lubbert, J. Duyster, T. Brummer, M. Boerries, T. Madl, B.R. Blazar, O. Gross, E.L. Pearce, R. Zeiser, Metabolic reprogramming of donor T cells enhances graft-versus-leukemia effects in mice and humans, Sci. Transl. Med. 12 (567) (2020).

[4] P.N. Desai, B. Wang, A. Fonseca, P. Borges, F.Z. Jelloul, P.K. Reville, E. Lee, C. Ly, A. Basi, J. Root, N. Baran, S.M. Post, Q. Deng, H. Sun, A.O. Harmanci, J.K. Burks, J. A. Gomez, C.D. DiNardo, N.G. Daver, G. Alatrash, M. Konopleva, M.R. Green, D. A. Antunes, A. Futreal, D. Hao, H.A. Abbas, Single-cell profiling of CD8+ T cells in acute myeloid leukemia reveals a continuous spectrum of differentiation and clonal hyperexpansion, Cancer Immunol. Res. (2023) OF1–OF18.

[5] C. Cerella, M. Dicato, M. Diederich, Enhancing personalized immune checkpoint therapy by immune archetyping and pharmacological targeting, Pharm. Res. 196 (2023) 106914.

[6] M. Ghandi, F.W. Huang, J. Jane-Valbuena, G.V. Kryukov, C.C. Lo, E.R. McDonald, 3rd, J. Barretina, E.T. Gelfand, C.M. Bielski, H. Li, K. Hu, A.Y. Andreev-Drakhlin, J. Kim, J.M. Hess, B.J. Haas, F. Aguet, B.A. Weir, M.V. Rothberg, B.R. Paolella, M. S. Lawrence, R. Akbani, Y. Lu, H.L. Tiv, P.C. Gokhale, A. de Weck, A.A. Mansour, C. Oh, J. Shih, K. Hadi, Y. Rosen, J. Bistline, K. Venkatesan, A. Reddy, D. Sonkin, M. Liu, J. Lehar, J.M. Korn, D.A. Porter, M.D. Jones, J. Golji, G. Caponigro, J. E. Taylor, C.M. Dunning, A.L. Creech, A.C. Warren, J.M. McFarland, M. Zamanighomi, A. Kauffmann, N. Stransky, M. Imielinski, Y.E. Maruvka, A. D. Cherniack, A. Tsherniak, F. Vazquez, J.D. Jaffe, A.A. Lane, D.M. Weinstock, C. M. Johannessen, M.P. Morrissey, F. Stegmeier, R. Schlegel, W.C. Hahn, G. Getz, G. B. Mills, J.S. Boehm, T.R. Golub, L.A. Garraway, W.R. Sellers, Next-generation characterization of the cancer cell line encyclopedia, Nature 569 (7757) (2019) 503–508.

[7] C. Cerella, S.R. Gajulapalli, A. Lorant, D. Gerard, F. Muller, Y. Lee, K.R. Kim, B. W. Han, C. Christov, C. Recher, J.E. Sarry, M. Dicato, M. Diederich, ATP1A1/BCL2L1 predicts the response of myelomonocytic and monocytic acute myeloid leukemia to cardiac glycosides, Leukemia 38 (1) (2024) 67–81.

[8] J. Gao, B.A. Aksoy, U. Dogrusoz, G. Dresdner, B. Gross, S.O. Sumer, Y. Sun, A. Jacobsen, R. Sinha, E. Larsson, E. Cerami, C. Sander, N. Schultz, Integrative analysis of complex cancer genomics and clinical profiles using the cBioPortal, Sci. Signal 6 (269) (2013) pl1.

[9] M.J. Goldman, B. Craft, M. Hastie, K. Repecka, F. McDade, A. Kamath, A. Banerjee, Y. Luo, D. Rogers, A.N. Brooks, J. Zhu, D. Haussler, Visualizing and interpreting cancer genomics data via the Xena platform, Nat. Biotechnol. 38 (6) (2020) 675–678.

[10] H. Bolouri, J.E. Farrar, T. Triche Jr., R.E. Ries, E.L. Lim, T.A. Alonzo, Y. Ma, R. Moore, A.J. Mungall, M.A. Marra, J. Zhang, X. Ma, Y. Liu, Y. Liu, J.M. Guidry Auvil, T.M. Davidsen, P. Gesuwan, L.C. Hermida, B. Salhia, S. Capone, G. Ramsingh, C.M. Zwaan, S. Noort, S.R. Piccolo, E.A. Kolb, A.S. Gamis, M. A. Smith, D.S. Gerhard, S. Meshinchi, The molecular landscape of pediatric acute myeloid leukemia reveals recurrent structural alterations and age-specific mutational interactions, Nat. Med. 24 (1) (2018) 103–112.

[11] C. McLeod, A.M. Gout, X. Zhou, A. Thrasher, D. Rahbarinia, S.W. Brady, M. Macias, K. Birch, D. Finkelstein, J. Sunny, R. Mudunuri, B.A. Orr, M. Treadway, B. Davidson, T.K. Ard, A. Chiao, A. Swistak, S. Wiggins, S. Foy, J. Wang, E. Sioson, S. Wang, J.R. Michael, Y. Liu, X. Ma, A. Patel, M.N. Edmonson, M.R. Wilkinson, A. M. Frantz, T.C. Chang, L. Tian, S. Lei, S.M.A. Islam, C. Meyer, N. Thangaraj, P. Tater, V. Kandali, S. Ma, T. Nguyen, O. Serang, I. McGuire, N. Robison, D. Gentry, X. Tang, L.E. Palmer, G. Wu, E. Suh, L. Tanner, J. McMurry, M. Lear, A. S. Pappo, Z. Wang, C.L. Wilson, Y. Cheng, S. Meshinchi, L.B. Alexandrov, M. J. Weiss, G.T. Armstrong, L.L. Robison, Y. Yasui, K.E. Nichols, D.W. Ellison, C. Bangur, C.G. Mullighan, S.J. Baker, M.A. Dyer, G. Miller, S. Newman, M. Rusch, R. Daly, K. Perry, J.R. Downing, J. Zhang, St. Jude Cloud: a pediatric cancer genomic data-sharing ecosystem, Cancer Discov. 11 (5) (2021) 1082–1099.

[12] D. Bottomly, N. Long, A.R. Schultz, S.E. Kurtz, C.E. Tognon, K. Johnson, M. Abel, A. Agarwal, S. Avaylon, E. Benton, A. Blucher, U. Borate, T.P. Braun, J. Brown, J. Bryant, R. Burke, A. Carlos, B.H. Chang, H.J. Cho, S. Christy, C. Coblentz, A. M. Cohen, A. d'Almeida, R. Cook, A. Danilov, K.T. Dao, M. Degnin, J. Dibb, C. A. Eide, I. English, S. Hagler, H. Harrelson, R. Henson, H. Ho, S.K. Joshi, B. Junio, A. Kaempf, Y. Kosaka, T. Laderas, M. Lawhead, H. Lee, J.T. Leonard, C. Lin, E. F. Lind, S.Q. Liu, P. Lo, M.M. Loriaux, S. Luty, J.E. Maxson, T. Macey, J. Martinez, J. Minnier, A. Monteblanco, M. Mori, Q. Morrow, D. Nelson, J. Ramsdill, A. Rofelty, A. Rogers, K.A. Romine, P. Ryabinin, J.N. Saultz, D.A. Sampson, S. L. Savage, R. Schuff, R. Searles, R.L. Smith, S.E. Spurgeon, T. Sweeney, R. T. Swords, A. Thapa, K. Thiel-Klare, E. Traer, J. Wagner, B. Wilmot, J. Wolf, G. Wu, A. Yates, H. Zhang, C.R. Cogle, R.H. Collins, M.W. Deininger, C.S. Hourigan, C. T. Jordan, T.L. Lin, M.E. Martinez, R.R. Pallapati, D.A. Pollyea, A.D. Pomicter, J. M. Watts, S.J. Weir, B.J. Druker, S.K. McWeeney, J.W. Tyner, Integrative analysis of drug response and clinical outcome in acute myeloid leukemia, Cancer Cell 40 (8) (2022) 850–864, e9.

[13] A. Maiga, S. Lemieux, C. Pabst, V.P. Lavallee, M. Bouvier, G. Sauvageau, J. Hebert, Transcriptome analysis of G protein-coupled receptors in distinct genetic subgroups of acute myeloid leukemia: identification of potential disease-specific targets, Blood Cancer J. 6 (6) (2016) e431.

[14] V.P. Lavallee, J. Chagraoui, T. MacRae, M. Marquis, A. Bonnefoy, J. Krosl, S. Lemieux, A. Marinier, C. Pabst, G.E. Rivard, J. Hebert, G. Sauvageau, Transcriptomic landscape of acute promyelocytic leukemia reveals aberrant surface expression of the platelet aggregation agonist Podoplanin, Leukemia 32 (6) (2018) 1349–1357.

[15] M. Marquis, C. Beaubois, V.P. Lavallee, M. Abrahamowicz, C. Danieli, S. Lemieux, I. Ahmad, A. Wei, S.B. Ting, S. Fleming, A. Schwarer, D. Grimwade, W. Grey, R. K. Hills, P. Vyas, N. Russell, G. Sauvageau, J. Hebert, High expression of HMGA2 independently predicts poor clinical outcomes in acute myeloid leukemia, Blood Cancer J. 8 (8) (2018) 68.

[16] I. Baccelli, Y. Gareau, B. Lehnertz, S. Gingras, J.F. Spinella, S. Corneau, N. Mayotte, S. Girard, M. Frechette, V. Blouin-Chagnon, K. Leveille, I. Boivin, T. MacRae, J. Krosl, C. Thiollier, V.P. Lavallee, E. Kanshin, T. Bertomeu, J. Coulombe-Huntington, C. St-Denis, M.E. Bordeleau, G. Boucher, P.P. Roux, S. Lemieux, M. Tyers, P. Thibault, J. Hebert, A. Marinier, G. Sauvageau, Mubritinib targets the electron transport chain complex I and reveals the landscape of OXPHOS dependency in acute myeloid leukemia, Cancer Cell 36 (1) (2019) 84–99, e8.

[17] G. Ehx, J.D. Larouche, C. Durette, J.P. Laverdure, L. Hesnard, K. Vincent, M. P. Hardy, C. Theriault, C. Rulleau, J. Lanoix, E. Bonneil, A. Feghaly, A. Apavaloaei, N. Noronha, C.M. Laumont, J.S. Delisle, L. Vago, J. Hebert, G. Sauvageau, S. Lemieux, P. Thibault, C. Perreault, Atypical acute myeloid leukemia-specific transcripts generate shared and immunogenic MHC class-I-associated epitopes, Immunity 54 (4) (2021) 737–752, e10.

[18] H. Kuusanmaki, O. Dufva, M. Vaha-Koskela, A.M. Leppa, J. Huuhtanen, I. Vanttinen, P. Nygren, J. Klievink, J. Bouhlal, P. Polonen, Q. Zhang, S. Adnan-Awad, C. Mancebo-Perez, J. Saad, J. Miettinen, K.K. Javarappa, S. Aakko, T. Ruokoranta, S. Eldfors, M. Heinaniemi, K. Theilgaard-Monch, U. Wartiovaara-Kautto, M. Keranen, K. Porkka, M. Konopleva, K. Wennerberg, M. Kontro, C. A. Heckman, S. Mustjoki, Erythroid/megakaryocytic differentiation confers BCL-XL dependency and venetoclax resistance in acute myeloid leukemia, Blood 141 (13) (2023) 1610–1625.

[19] D. Aran, A.P. Looney, L. Liu, E. Wu, V. Fong, A. Hsu, S. Chak, R.P. Naikawadi, P. J. Wolters, A.R. Abate, A.J. Butte, M. Bhattacharya, Reference-based analysis of lung single-cell sequencing reveals a transitional profibrotic macrophage, Nat. Immunol. 20 (2) (2019) 163–172.

[20] R.G. Verhaak, B.J. Wouters, C.A. Erpelinck, S. Abbas, H.B. Beverloo, S. Lugthart, B. Lowenberg, R. Delwel, P.J. Valk, Prediction of molecular subtypes in acute myeloid leukemia based on gene expression profiling, Haematologica 94 (1) (2009) 131–134.

[21] A. Tsherniak, F. Vazquez, P.G. Montgomery, B.A. Weir, G. Kryukov, G.S. Cowley, S. Gill, W.F. Harrington, S. Pantel, J.M. Krill-Burger, R.M. Meyers, L. Ali, A. Goodale, Y. Lee, G. Jiang, J. Hsiao, W.F.J. Gerath, S. Howell, E. Merkel, M. Ghandi, L.A. Garraway, D.E. Root, T.R. Golub, J.S. Boehm, W.C. Hahn, Defining a cancer dependency map, Cell 170 (3) (2017) 564–576, e16.

[22] S.B. Hay, K. Ferchen, K. Chetal, H.L. Grimes, N. Salomonis, The human cell atlas bone marrow single-cell interactive web portal, Exp. Hematol. 68 (2018) 51–61.

[23] S.X. Ge, D. Jung, R. Yao, ShinyGO: a graphical gene-set enrichment tool for animals and plants, Bioinformatics 36 (8) (2020) 2628–2629.

[24] D. Aran, Z. Hu, A.J. Butte, xCell: digitally portraying the tissue cellular heterogeneity landscape, Genome Biol. 18 (1) (2017) 220.

[25] A.H. Maag, H. Swanton, M. Kull, N.M. Vegi, M. Feuring, Immunophenotypical profiling of myeloid neoplasms with erythroid predominance using mass cytometry (CyTOF), Cytom. A 103 (7) (2023) 551–562.

[26] M.J. Ailia, J. Heo, S.Y. Yoo, Navigating through the PD-1/PDL-1 landscape: a systematic review and meta-analysis of clinical outcomes in hepatocellular carcinoma and their influence on immunotherapy and tumor microenvironment, Int J. Mol. Sci. 24 (7) (2023).

[27] A. Warren, Y. Chen, A. Jones, T. Shibue, W.C. Hahn, J.S. Boehm, F. Vazquez, A. Tsherniak, J.M. McFarland, Global computational alignment of tumor and cell line transcriptional profiles, Nat. Commun. 12 (1) (2021) 22.
[28] P. Jiang, S. Gu, D. Pan, J. Fu, A. Sahu, X. Hu, Z. Li, N. Traugh, X. Bu, B. Li, J. Liu, G. J. Freeman, M.A. Brown, K.W. Wucherpfennig, X.S. Liu, Signatures of T cell dysfunction and exclusion predict cancer immunotherapy response, Nat. Med. 24 (10) (2018) 1550–1558.
[29] C. Cerella, A. Gaigneaux, A. Mazumder, J.Y. Lee, E. Saland, F. Radogna, T. Farge, F. Vergez, C. Recher, J.E. Sarry, K.W. Kim, H.Y. Shin, M. Dicato, M. Diederich, Bcl-2 protein family expression pattern determines synergistic pro-apoptotic effects of BH3 mimetics with hemisynthetic cardiac glycoside UNBS1450 in acute myeloid leukemia, Leukemia 31 (3) (2017) 755–759.
[30] A. Mazumder, J.Y. Lee, O. Talhi, C. Cerella, S. Chateauvieux, A. Gaigneaux, C. R. Hong, H.J. Kang, Y. Lee, K.W. Kim, D.W. Kim, H.Y. Shin, M. Dicato, K. Bachari, A.M.S. Silva, B. Orlikova-Boyer, M. Diederich, Hydroxycoumarin OT-55 kills CML cells alone or in synergy with imatinib or Synribo: Involvement of ER stress and DAMP release, Cancer Lett. 438 (2018) 197–218.
[31] I. Terren, A. Orrantia, J. Vitalle, O. Zenarruzabeitia, F. Borrego, CFSE dilution to study human T and NK cell proliferation in vitro, Methods Enzym. 631 (2020) 239–255.
[32] D.P. Nusinow, J. Szpyt, M. Ghandi, C.M. Rose, E.R. McDonald, 3rd, M. Kalocsay, J. Jane-Valbuena, E. Gelfand, D.K. Schweppe, M. Jedrychowski, J. Golji, D. A. Porter, T. Rejtar, Y.K. Wang, G.V. Kryukov, F. Stegmeier, B.K. Erickson, L. A. Garraway, W.R. Sellers, S.P. Gygi, Quantitative proteomics of the cancer cell line encyclopedia, Cell 180 (2) (2020) 387–402, e16.
[33] A.J. Combes, B. Samad, J. Tsui, N.W. Chew, P. Yan, G.C. Reeder, D. Kushnoor, A. Shen, B. Davidson, A.J. Barczak, M. Adkisson, A. Edwards, M. Naser, K.C. Barry, T. Courau, T. Hammoudi, R.J. Arguello, A.A. Rao, A.B. Olshen, C. Immunoprofiler, C. Cai, J. Zhan, K.C. Davis, R.K. Kelley, J.S. Chapman, C.E. Atreya, A. Patel, A. I. Daud, P. Ha, A.A. Diaz, J.R. Kratz, E.A. Collisson, G.K. Fragiadakis, D.J. Erle, A. Boissonnas, S. Asthana, V. Chan, M.F. Krummel, Discovering dominant tumor immune archetypes in a pan-cancer census, Cell 185 (1) (2022) 184–203, e19.
[34] D.A. Sallman, A.F. McLemore, A.L. Aldrich, R.S. Komrokji, K.L. McGraw, A. Dhawan, S. Geyer, H.A. Hou, E.A. Eksioglu, A. Sullivan, S. Warren, K. J. MacBeth, M. Meggendorfer, T. Haferlach, S. Boettcher, B.L. Ebert, N.H. Al Ali, J. E. Lancet, J.L. Cleveland, E. Padron, A.F. List, TP53 mutations in myelodysplastic syndromes and secondary AML confer an immunosuppressive phenotype, Blood 136 (24) (2020) 2812–2823.
[35] A.M. Zeidan, I. Boss, C.L. Beach, W.B. Copeland, E. Thompson, B.A. Fox, V.E. Hasle, K. Ogasawara, J. Cavenagh, L.R. Silverman, M.T. Voso, A. Hellmann, M. Tormo, T. O'Connor, A. Previtali, S. Rose, G. Garcia-Manero, A randomized phase 2 trial of azacitidine with or without durvalumab as first-line therapy for higher-risk myelodysplastic syndromes, Blood Adv. 6 (7) (2022) 2207–2218.
[36] H. Dohner, A.H. Wei, F.R. Appelbaum, C. Craddock, C.D. DiNardo, H. Dombret, B. L. Ebert, P. Fenaux, L.A. Godley, R.P. Hasserjian, R.A. Larson, R.L. Levine, Y. Miyazaki, D. Niederwieser, G. Ossenkoppele, C. Rollig, J. Sierra, E.M. Stein, M. S. Tallman, H.F. Tien, J. Wang, A. Wierzbowska, B. Lowenberg, Diagnosis and management of AML in adults: 2022 recommendations from an international expert panel on behalf of the ELN, Blood 140 (12) (2022) 1345–1377.
[37] H. Long, Q. Jia, L. Wang, W. Fang, Z. Wang, T. Jiang, F. Zhou, Z. Jin, J. Huang, L. Zhou, C. Hu, X. Wang, J. Zhang, Y. Ba, Y. Gong, X. Zeng, D. Zeng, X. Su, P. B. Alexander, L. Wang, L. Wang, Y.Y. Wan, X.F. Wang, L. Zhang, Q.J. Li, B. Zhu, Tumor-induced erythroid precursor-differentiated myeloid cells mediate immunosuppression and curtail anti-PD-1/PD-L1 treatment efficacy, Cancer Cell 40 (6) (2022) 674–693, e7.
[38] A.T. Gerds, B.L. Scott, P. Greenberg, T.L. Lin, D.A. Pollyea, A. Verma, M. Dail, Y. Feng, C. Green, C. Ma, B.C. Medeiros, M. Yan, K. Yousefi, W. Donnellan, Atezolizumab alone or in combination did not demonstrate a favorable risk-benefit profile in myelodysplastic syndrome, Blood Adv. 6 (4) (2022) 1152–1161.
[39] H. Mumme, B.E. Thomas, S.S. Bhasin, U. Krishnan, B. Dwivedi, P. Perumalla, D. Sarkar, G.B. Ulukaya, H.S. Sabnis, S.I. Park, D. DeRyckere, S.S. Raikar, M. Pauly, R.J. Summers, S.M. Castellino, D.S. Wechsler, C.C. Porter, D.K. Graham, M. Bhasin, Single-cell analysis reveals altered tumor microenvironments of relapse- and remission-associated pediatric acute myeloid leukemia, Nat. Commun. 14 (1) (2023) 6209.